Spectrophotometry of the Khonsu region on the comet 67P/Churyumov–Gerasimenko using OSIRIS instrument images

J. D. P. Deshapriya,[1][*] M. A. Barucci,[1][*] S. Fornasier,[1][*] C. Feller,[1] P. H. Hasselmann,[1] H. Sierks,[2] M.R. El-Maarry,[3] M. Pajola,[4] C. Barbieri,[5] P. L. Lamy,[6] R. Rodrigo,[7,8] D. Koschny,[9] H. Rickman,[10,11] J. Agarwal,[2] M. F. A'Hearn,[12] J.-L. Bertaux,[13] I. Bertini,[5] S. Boudreault,[2] G. Cremonese,[14] V. Da Deppo,[15] B. J. R. Davidsson,[16] S. Debei,[17] J. Deller,[2] M. De Cecco,[18] M. Fulle,[19] A. Gicquel,[2] O. Groussin,[6] P. J. Gutierrez,[20] C. Güttler,[2] M. Hofmann,[2] S. F. Hviid,[21] W. Ip,[22] L. Jorda,[6] H. U. Keller,[23] J. Knollenberg,[21] R. Kramm,[2] E. Kührt,[21] M. Küppers,[24] L. Lara,[20] M. Lazzarin,[5] J.J. Lopez Moreno,[20] F. Marzari,[5] S. Mottola,[21] G. Naletto,[15,25,26] N. Oklay,[2] D. Perna,[1] A. Pommerol,[3] N. Thomas,[3] C. Tubiana[2] and J.-B. Vincent[2]

Affiliations are listed at the end of the paper

ABSTRACT

Our work focuses on the spectrophotometric analysis of selected terrain and bright patches in the Khonsu region on the comet 67P/Churyumov–Gerasimenko. Despite the variety of geological features, their spectrophotometric properties appear to indicate a similar composition. It is noticeable that the smooth areas in Khonsu possess similar spectrophotometric behaviour to some other regions of the comet. We observed bright patches on Khonsu with an estimation of >40 per cent of normal albedo and suggest that they are associated with H_2O ice. One of the studied bright patches has been observed to exist on the surface for more than 5 months without a major decay of its size, implying the existence of potential sub-surface icy layers. Its location may be correlated with a cometary outburst during the perihelion passage of the comet in 2015 August, and we interpret it to have triggered the surface modifications necessary to unearth the stratified icy layers beneath the surface. A boulder analysis on Khonsu leads to a power-law index of $-3.1 +0.2/-0.3$ suggesting a boulder formation, shaped by varying geological processes for different morphological units.

Key words: techniques: photometric – comets: individual: 67P/Churyumov-Gerasimenko.

1 INTRODUCTION

The Rosetta spacecraft rendezvoused with the comet 67P/Churyumov–Gerasimenko (hereafter 67P/C-G) in 2014 August and has been following the comet towards the later phases of the mission, producing copious amounts of scientific data. The Optical, Spectroscopic and Infrared Remote Imaging System (OSIRIS), aboard Rosetta has been very useful to characterise the cometary nucleus in exceptional detail. With OSIRIS's eyes, namely Narrow Angle Camera (NAC) and Wide Angle Camera (WAC), it has been possible to study a very irregular object with

a low visible albedo, featuring a variety of locally heterogeneous morphologies. Although previous visits to comets, all of which were fly-by missions, expanded our understanding (Barucci, Dotto & Levasseur-Regourd 2011) about comets, the OSIRIS imaging instrument (Keller et al. 2007) has furthered this research by allowing us to follow the temporal evolution of the comet continuously and to image the cometary nucleus in unprecedented spatial resolution. The NAC is equipped with 11 broad-band filters centred at different wavelengths from 269 through 989 nm with the intention of studying the cometary nucleus, whereas the WAC is dedicated to the study of gaseous species in the coma with 14 narrow-band filters centred at wavelengths ranging from 246 to 631 nm. OSIRIS has been mapping the cometary surface at numerous observing conditions and has been able to reach a spatial
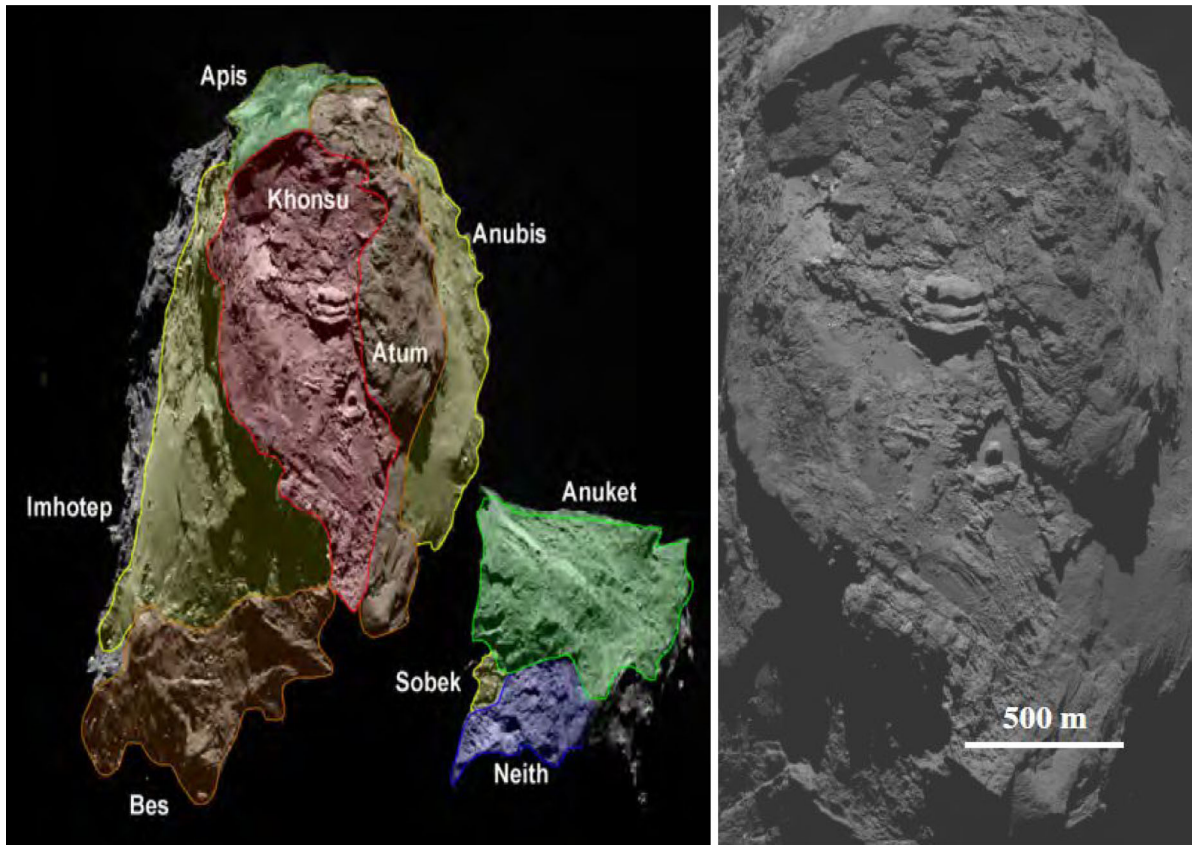
Figure 1. Left: image of the whereabouts of the Khonsu region on the bilobate nucleus with respect to boundaries of the visible regions overlaid with their names annotated (El-Maarry et al. 2016), right: a zoomed view on the Khonsu region.

resolution of 11 cm per pixel during the fly-by of 2015 February 14 as Rosetta hovered just 6 km above the cometary surface. It is noteworthy that at a distance of 100 km, NAC has a spatial resolution of 1.86 m per pixel, while that of WAC is 10.1 m per pixel at the same distance.

Since Rosetta's arrival at the comet, OSIRIS has been carrying out observations under careful scrutiny as the comet was approaching the perihelion of its orbit. In 2015 August, during the perihelion passage, Rosetta was obliged to recede from the comet due to its enhanced activity as a precautionary measure. However around 2015 December, Rosetta returned to the vicinity of the comet and resumed high-resolution observations and is expected to continue through the end of 2016 September, which will mark the end of the extended mission.

OSIRIS observations have revealed a bilobate nucleus accreted from a pair of cometesimals each having an irregular shape, despite sharing similar stratifications (Massironi et al. 2015). The Northern hemisphere of the comet has been examined in much detail with the identification of a plethora of geomorphological features (Sierks et al. 2015, Thomas et al. 2015), whereas the Southern hemisphere of the comet got exposed to the sun light later on. With the illumination conditions favouring the detailed mapping of Southern hemisphere of the comet, 2015 May marked a cornerstone of the Rosetta mission as more southern regions of the comet fell into the visibility, thus allowing us to expand the existing mapping phases that had previously been restricted to the Northern hemisphere. This opened the possibility to explore and characterise the southern regions on the cometary nucleus that would be freshly exposed to the sun light after a long winter. Subsequently following

the observations, a number of regions were identified in the Southern hemisphere with a diversity of geological features (El-Maarry et al. 2016). The Khonsu region (see Fig. 1), in particular, is unique due to its geomorphology and spectrophotometric properties with prominent bright spots (Barucci et al. 2016) observed therein. The Khonsu region started to be observed by the OSIRIS imaging instrument from 2015 March onwards through the perihelion passage of the comet in 2015 August and beyond. Khonsu displays both smooth and rough terrain with a large quantity of boulders and irregular outcrops. It has pronounced steep boundaries with neighbouring Atum and Apis regions, marked by numerous boulders that might be what remains following a formation, basically through cliff collapse (El-Maarry et al. 2016). Towards the west, Khonsu leads gradually to the smooth areas of Imhotep region and touches Bes region to the south (we refer to El-Maarry et al. 2015 for the nomenclature and definitions of the northern regions of the comet 67P/C-G). Although a considerable amount of work has been done covering many other regions of the comet, Khonsu has not been previously explored in detail. On the other hand, this is also a region that has started to be freshly exposed to the sun following the long winter in the Southern hemisphere of the comet and studying Khonsu since its early stages of illumination in its current orbit could allow us to follow the potential variations of spectrophotometric properties of different surface features. The background of this work focuses on investigating the manifold morphological features observed in this unique region by exploring their spectrophotometric properties using the images that have been recorded from 2015 March up to 2016 June. OSIRIS NAC images have been used for this work, unless otherwise specified, in the case of WAC.

Table 1. Observational parameters of the surface feature comparison

ID	Time	Altitude (km)	*S/R* (m/pixel)	Heliocentric distance (au)	Phase angle	Pixel box dimensions
1	2015-05-02_15h09 UTC	123.28	2.29	1.72	60°.48	7×7
2	2016-02-10_11h53 UTC	48.00	0.89	2.33	65°.20	18×18

2 DATA REDUCTION

The data used for this study are sourced from the level 3B of the OSIRIS standard pipeline where they have undergone the data reductions described in Küppers et al. (2007) and Tubiana et al. (2015). These account for the correction of bias, flat-field, geometric distortion and calibration in absolute flux up to the level 3 of the pipeline and data are available in spectral radiance in the format of $W sr^{-1} m^{-2} nm^{-1}$. In the level 3B, the data are then converted into the radiance factor $\pi.(I/F)$ using equation (1):

$$Radiance factor(I/F) = \frac{\pi I(i, e, \alpha, \lambda)}{F(\lambda)}, \quad (1)$$

Here I is referred to as the observed scattered spectral radiance, whereas F is the solar spectral irradiance at the heliocentric distance of the comet. The symbols i, e, α and λ correspond to the incident angle, emission angle, phase angle and wavelength, respectively. It is noteworthy that solar irradiance has been calculated at the central wavelength of each filter in order to be consistent with the derivation of the absolute calibration factors.

When OSIRIS is in operation during a multispectral observational sequence, the images are recorded successively and usually, there is a delay of about 10–15 s between each pair of consecutive images and there is also the movement of both the spacecraft and the comet, which translates into a slight shift of the fields of view between a given pair of consecutive images. The shift becomes more pronounced when the spacecraft is closer to the cometary nucleus as this is when the spacecraft will be moving faster. Therefore, this effect translates into the requirement of co-registering the images of the observational sequence in order to perform spectrophotometry. We treat this problem by adapting an algorithm that automatically identifies identical features in consecutive images and estimates the projective transformation matrix between each pair of consecutive images (ORB and RANSAC tools implemented by van der Walt et al. 2014), leading to an adequate alignment of the images. This co-registration of images results in a multispectral data cube on which the spectral analyses can be carried out.

Next, we corrected the different illumination conditions that prevailed during the observations by using Lommel–Seeliger disc law (Fairbairn 2005), which is appropriate for this case, given the low-albedo nature of the comet 67P/C-G. The disc function, D, is defined in equation (2) where i and e stand for incident and emission angles for a given pixel:

$$D(i, e) = \frac{2 \cos(i)}{\cos(i) + \cos(e)}. \quad (2)$$

We retrieved these angles by generating synthetic images for a given set of observational conditions using the shape model SHP5 (Jorda et al. 2016) together with Optimized Astrophysical Simulator for Imaging Systems simulator (Jorda et al. 2010) that relies on Rosetta SPICE kernels (Acton 1996) in order to obtain the ephemeris for the observations in question. Then, the correction is achieved by taking the ratio between the previously calculated radiance factor and the disc function (equation 3):

$$I/F_{corrected} = \frac{\pi I(i, e, \alpha, \lambda)}{F(\lambda)D(i, e)}. \quad (3)$$

Once this illumination correction is applied over the multispectral data cube, it is possible to perform the spectrophotometric analysis. In this context, we restrict our scope to the observational sequences featuring Khonsu region. Thus, using the data cube, we plot the corrected radiance factor for areas of interest against the wavelength. This allows the visualisation of the spectrophotometric curve of the selected areas and compare different morphological features on the surface, which could give insights about albedo properties of the selected areas. In addition, we provide relative reflectance plots where we have normalised the corrected radiance factor values to a given filter. We used the OSIRIS NAC F23 green filter, centred at 535.7 nm to be consistent with similar analyses performed by Fornasier et al. (2015), Barucci et al. (2016) and Oklay et al. (2016).

3 ANALYSIS OF DIFFERENT SURFACE FEATURES IN KHONSU
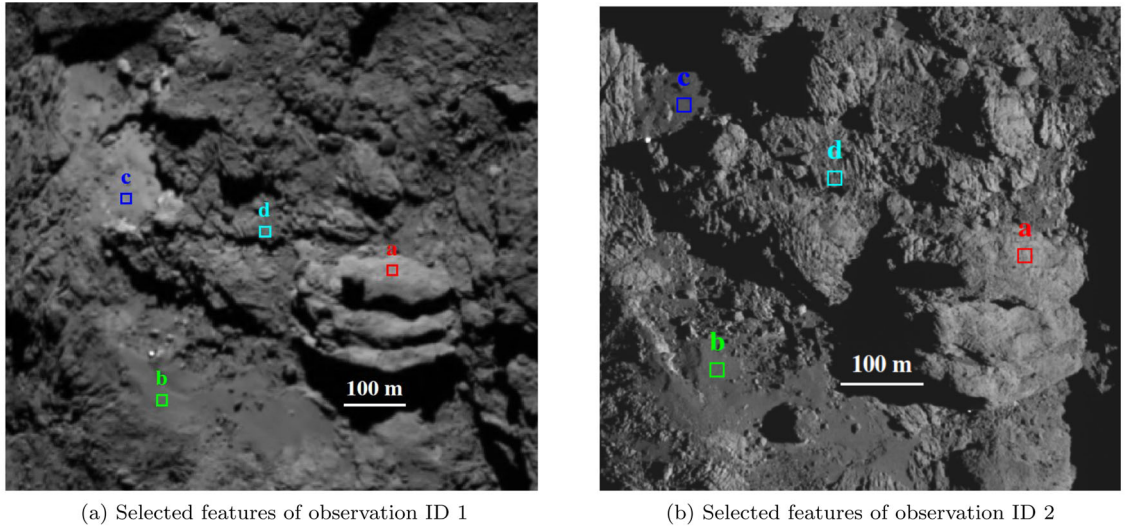
3.1 Spectrophotometry

In order to investigate the surface properties of the Khonsu region, we selected four different types of surface features (we refer to El-Maarry et al. 2016 for a dedicated description of the terrain) observed at two different periods and studied their spectrophotometric behaviour. The observational parameters are given in the Table 1 for both cases and here we use illumination-corrected and properly co-registered multispectral cubes.

We defined the four regions of interest over the following surface features shown in Figs 2(a) and 2(b) where the definitions are made with boxes of 7×7 pixels and 18×18 pixels, respectively:

(a) part of the 'pancake' feature,
(b) dark smooth terrain,
(c) light smooth terrain,
(d) rugged terrain.

The selection of different box dimensions corresponds directly to the different spatial resolutions of the two observations and the necessity to cover an area that is large enough to contain the local physiographic varieties that are being studied.

Both multispectral cubes are prepared with 11 NAC filters and for each of the observations, we plot the median of our four samples containing the corrected radiance factor, against the filter wavelengths per each selected surface feature and perform a normalisation at 535.7 nm for the relative reflectance plot. The subsequent plots are depicted in Figs 2(c) and 2(d). From the observation ID 1, it is evident that the light smooth terrain displays the highest reflectance among the features considered, whereas the rugged terrain corresponds to the lowest reflectance. Although these features show subtle variations in their reflectance characteristics, they all share a red spectral behaviour. From the spectrophotometric curves of the observation ID 2, it is clear that the highest reflectance is shared by the part of the pancake feature and dark smooth terrains. A comparison of reflectance curves between the two observations suggests that some of the selected features have undergone a variation of reflectance between the two periods. The order of reflectances of all the features has been affected, except for the rugged terrain that
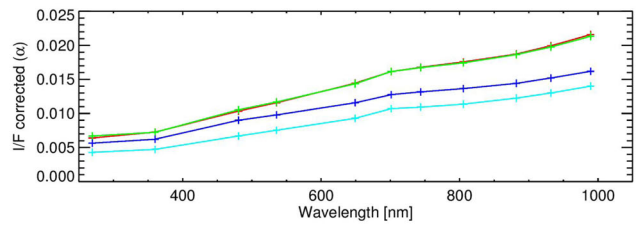
(a) Selected features of observation ID 1

(b) Selected features of observation ID 2
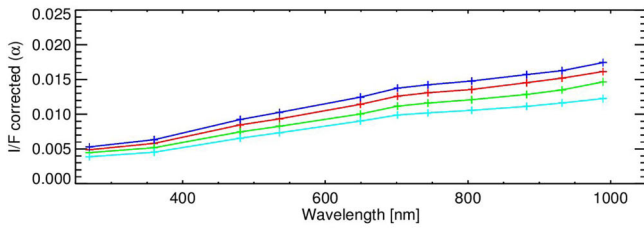
(c) Spectrophotometric plots for the selected features of obs. ID 1

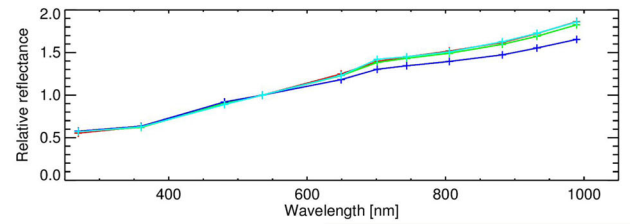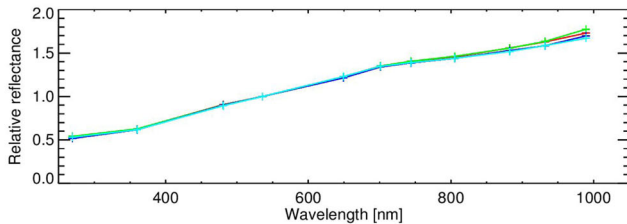(d) Spectrophotometric plots for the selected features of obs. ID 2

Figure 2. Spectrophotometric analysis for different surface features in Khonsu region. The boxes in Fig. 2(a) have dimensions of 7×7 pixels, while those in Fig. 2(b) have 18×18 pixels as dimensions.

has remained with the lowest reflectance in both observations. This observation could be explained in the way that there was increased cometary activity during the perihelion passage (2015 August) that occurred between the two observational periods and that it has lifted off some of the dust sitting on the cometary surface (Fornasier et al. 2016). Fresh material with higher reflectance could have thus been exposed in the smooth terrain during the perihelion passage, as observed in 2016 February. On the other hand, rugged terrain, composed of condensed cometary material, does not seem to have been affected, as it is probably resistant to the same kind of cometary activity that refreshed the surface of smooth terrains.

We computed the spectral slopes (see Table 2) for each of the four pre-defined surface features, integrating the signal over the boxes of identical pixel dimensions, following the definition in equation (4), where R882.1 and R535.7 are radiance factors for a given pixel for the corresponding filters (centred at 882.1 and 535.7 nm). We compute the mean spectral slope value from the integrated flux over a given box, excluding the contribution from pixels located in shadows. Generally, spectral slopes are helpful to quantify and compare colour variations of surfaces. For instance, they have been used to explore global colours of the comet (Fornasier et al. 2015),

to analyse the selected landing site Agilkia (La Forgia et al. 2015) for the Philae lander, to study the landing site candidate A (Pajola et al. 2015), to characterise the landing site Abydos (Lucchetti et al. 2016) and to carry out a variegation analysis of the active regions of the comet (Oklay et al. 2016). The spectral slope values for each of the above features are presented mainly because of the local heterogeneities of the terrain. A general estimate for entire terrain is given in Table 2 for the sake of the statistics, which should be given special care due to the plethora of surface features in the Khonsu region and we would encourage the use of local individual spectral slope values when comparing.

SpectralSlope[per cent/100 nm]

$$= \frac{(R_{882.1}(\alpha) - R_{535.7}(\alpha))(10000)}{R_{535.7}(\alpha)(882\,\text{nm} - 535\,\text{nm})}. \qquad (4)$$

With the obtained spectral slope values for the given phase angles, we can associate Khonsu region to the 'average spectral group' among the three spectral slope groups introduced by Fornasier et al. (2015). This average spectral slope group is defined between 14 and 18%/(100 nm) at a phase angle around 50°, and the Anuket

Table 2. Spectral slope values for the selected four surface features (Figs 2a and 2b) on Khonsu region during two observational sequences. Spectral slopes are evaluated for per cent/100 nm in the 882–535 nm range using boxes of 7×7 pixels and 18×18 pixels for the observations on 2015 May 2 and 2016 February 10, respectively. The difference of the sampling is due to the different spatial resolutions of two scenarios and the sizes of both of the boxes translate to 16×16 m^2 on the surface. The errors are calculated from the distribution of pixels defined for each feature. For example, in the case of a feature of the observation on 2015 May 2, the standard deviation of the 7×7 pixels is used as the error. As for the observation on 2016 February 10, it is the standard deviation of a sample of 18×18 pixels, except for the ID d, where the sample is a filtered 250 pixels from the default 18×18 pixels in order to avoid the pixels affected from the shadows.

ID	Surface feature	Spectral slope 2015 May 2 at phase $\sim 60°$	Error($\pm$)	Spectral slope 2016 February 10 at phase $\sim 65°$	Error($\pm$)
a	Part of the 'pancake' feature	15.92	0.67	17.96	0.76
b	Dark smooth terrain	15.96	0.43	17.16	0.51
c	Light smooth terrain	14.96	1.04	13.53	0.91
d	Rugged terrain	15.28	0.98	17.35	0.92
	Mean	15.53	0.40	16.50	0.39

and Serqet regions of the comet belong to this spectral slope group. Furthermore, in comparison with the work done by Oklay et al. (2016), the terrain analysed here corresponds to their 'higher spectral slope' group, defined above 15%/(100 nm) and this group is associated with inactive regions. The aforementioned red spectral behaviour has been associated with the presence of organic compounds in the comet by Capaccioni et al. (2015) using VIRTIS spectro-imager on-board Rosetta, which operates from 0.25 to 5 μm. The relative reflectance plots shown in Figs 2(c) and 2(d) yield that all the selected surfaces features show similar composition as their normalised curves almost coincide. The deviation of the relative reflectance curve in near-infrared wavelenghts, shown by the light smooth terrain in Fig. 2(d) can be attributed to the presence of the bluish material on the surface. We interpret the spectral behaviour of the selected features on the Khonsu surface to be consistent with the spectral behaviour of the typical nucleus of 67P/C-G as demonstrated in Barucci et al. (2016) and Fornasier et al. (2015).

In Fig. 3, we visualise a few RGB (Red, green, blue filters) images for different observing conditions, realised using STIFF program (Bertin 2011), which produces colour images from astronomical data. These images reveal the presence of some bluish material (compared to the surroundings) on the surface of the Khonsu region during these observations corresponding to varying periods of Rosetta's escorting phase of the mission. Fig. 3(b), dated 2015 July 26, shows the abundance of the bluish material on the comet with an oblique view on Khonsu that relates to a period of about two weeks before the perihelion passage of the comet where the cometary activity progressively removed a part of the dust mantle, revealing fresh surface underneath (Fornasier et al. 2016). The same image also illustrates a transient cometary outburst, attributed to the increased cometary activity and this has been identified (ID 3) as a type-B outburst by Vincent et al. (2016). Fig. 3(d) shows a narrow field of view of the Khonsu region at a better spatial resolution with the presence of the bluish material. Several blue patches are identifiable and the associated spectrophotometric plots are presented in Fig. 4 which shows that this bluish material follows the general relative reflectance behaviour of the nucleus at near-ultraviolet wavelengths, whereas its relative reflectance seems to have lowered at near-infrared wavelengths. We computed the spectral slope for this bluish material, evaluated as the mean for a 20×20 pixels square box to be about 11%/100 nm (phase angle $\sim 65°$) according to the definition established earlier. A similar behaviour corresponding to a lower spectral slope has been found on the regions of 'lower spectral slope' group introduced by Fornasier et al. (2015). This lower spectral slope ranges from 11 to 14%/(100 nm) at a phase angle around $50°$ and includes Hapi, Hathor and Seth regions. This

spectrophotometric behaviour has been attributed to a higher abundance of H_2O ice mixed with the desiccated refractory material. With the work done by Oklay et al. (2016) in mind, this bluish material corresponds to the 'low spectral slope' group ranging from 8 to 13%/(100 nm) and can be potentially associated with some sources of activity, being active pits, alcoves, bright features and, in particular, the Hapi region.

According to the spectral slope comparison presented in Table 2 for the two aforementioned observations at phase angles $\sim 60°$ and $\sim 65°$, we noticed a slight phase-reddening effect for three out of four surface features considered. The only surface feature that does not show phase-reddening is the 'light smooth terrain' whose spectral slope diminishes as the phase angle increases. Although this seems an outlier at first glance, this deviation could be explained by the presence of bluish material, which dominates the spectral slope in the observation on 2016 February 10. The RGB image on Fig. 3(d) makes this more evident. From the above statistics, a slope of 0.35 ± 0.12%/(100 nm)/deg can be obtained, discarding the 'light smooth terrain' where a phase-reddening is absent. We also note that using OSIRIS observations, Fornasier et al. (2015) obtained disc-averaged spectral slopes, increasing from 11%/(100 nm) to 16%/(100 nm) in the $1°.3$–$54°$ phase angle range, leading to approximately 0.1%/(100 nm)/deg. Using VIRTIS data spread between $20°$ and $120°$ of phase angles, Ciarniello et al. (2015) obtained 0.07%/(100 nm)/deg in the wavelength range from 550 to 800 nm. The data of the aforementioned studies are sourced to pre-perihelion period of the comet (Fornasier et al. – 2014 July/August and Ciarniello et al. – from 2014 July to 2015 February), when 67P/C-G was in an inbound orbit at heliocentric distances of about 3 au. The results of Fornasier et al. (2015) correspond to the mean spectral slope of the entire nucleus, whereas our results are more specific to the analysed features of the Khonsu region, which demonstrate heterogeneous characteristics. However, as explained in Fornasier et al. (2016), the comet's sub-surface has been partially exposed, approaching the perihelion, as the increasing level of cometary activity has removed parts of the dust mantle, which results in the variation of the spectral slope.

3.2 Boulder analysis

Considering that a large quantity of boulders are present in Khonsu region, we decided to analyse the boulder distribution in order to get an insight into what might have been the origins of their formation. We used the observations made on 2015 May 2 when Rosetta was at ~ 125 km from the comet, and identified the physiographic region of Khonsu (see Fig. 1). The resulting scale of 2.3 m pixel^{-1} of
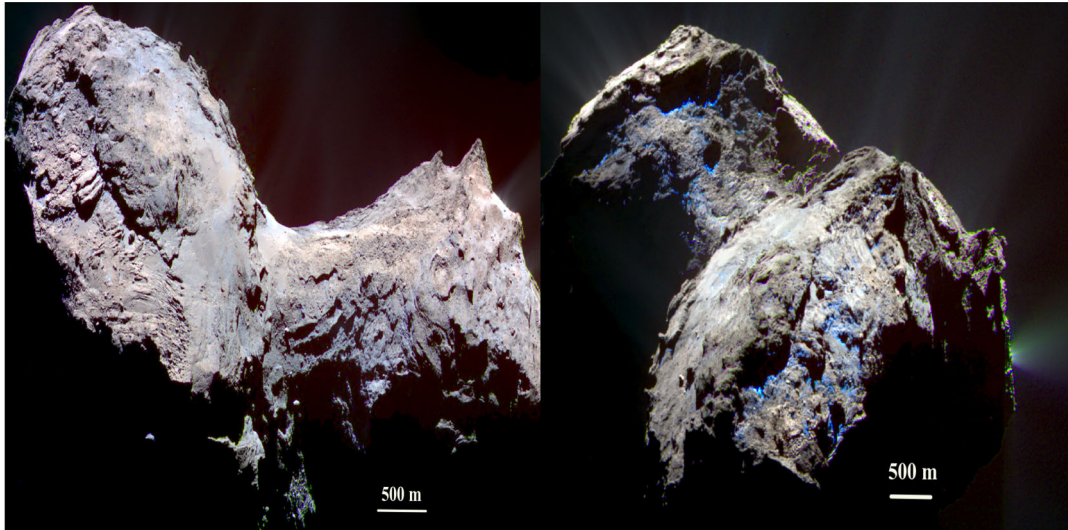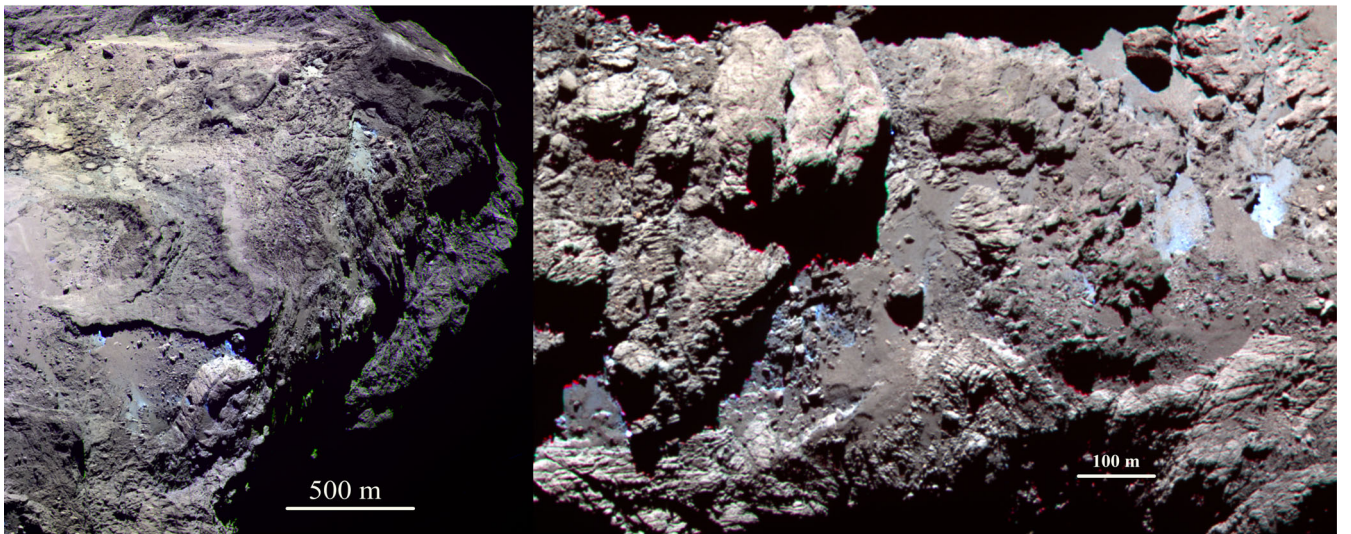
(a) 2015-05-02_13h42 2.29 m/pixel $\alpha = 60.62\,^\circ$ (b) 2015-07-26_20h22 3.09 m/pixel $\alpha = 89.88\,^\circ$

(c) 2016-01-27_14h10 1.30 m/pixel $\alpha = 62.67\,^\circ$ (d) 2016-02-10_11h53 0.89 m/pixel $\alpha = 65.21\,^\circ$

Figure 3. RGB images featuring Khonsu region and some of its neighbourhood. For the red, green and blue colours, OSIRIS NAC images with filter wavelengths centred at 882.1, 649.2 and 480.7 nm have been used, respectively. Some images have been cropped to better highlight the details pertaining to Khonsu region. The red and green features that sometimes appear adjacent to the shadows are artefacts arising from the imperfect co-registration/receding shadows of the images.

the used NAC image presented the possibility to derive meaningful statistics for boulders with diameters ≥7 m, the 3 pixels sampling that minimises the likelihood of misidentifications of what we are observing (Nyquist 1928). Since the observations were performed with a phase angle $\alpha \sim 62^\circ$, the presence of elongated shadows on the surface aided with the identification of even smaller boulders (2 pixels diameter, ~4–5 m) (Pajola et al. 2015, 2016a). We did not include these smaller populations in the cumulative size–frequency distribution (SFD), because they do not represent a complete data set for such small sizes. Before performing the boulder counting, we defined the positive reliefs detectable in multiple images as 'boulders', obtained with different observation geometries with the constant presence of an elongated shadow (if $\alpha > 0^\circ$) whose extension depends on the illumination geometry (Pajola et al. 2015, 2016a). We then manually identified such features on the image using the ARCGIS software as done in Pajola et al. (2016a) and measured their position on the surface of the comet, assuming a spherical shape. We

present here a physiographic boulder analysis of the Khonsu region for the boulders extracted from the entire boulder data set of Pajola et al. (2016b). Eventually, to obtain the cumulative boulder SFD per km^2, we used the corresponding area of 1.705 km^2 computed from the 3D shape model of the comet (Jorda et al. 2016).

The total number of identified boulders ≥7 m is 471 (69 being in the 6 m bin, 49 in the 5 m bin, 27 in the 4 m bin and 6 boulders in the 3 m bin). We consequently plotted the cumulative binned number of boulders versus boulder size in metres (Fig. 5). We obtained the power-law index of −3.1 +0.2/−0.3, by fitting a continuous regression line to the data in the range of 7–40 m. The cumulative number of boulders ≥7 m per km^2 derived on this area is 276, which is 2.8 times the number derived on the entire northern and equatorial regions of the comet (Pajola et al. 2015), while completely comparable to the value obtained on the Southern hemisphere (Pajola et al. 2016b). In order to understand what this index reveals about the possible processes that produced and modified the
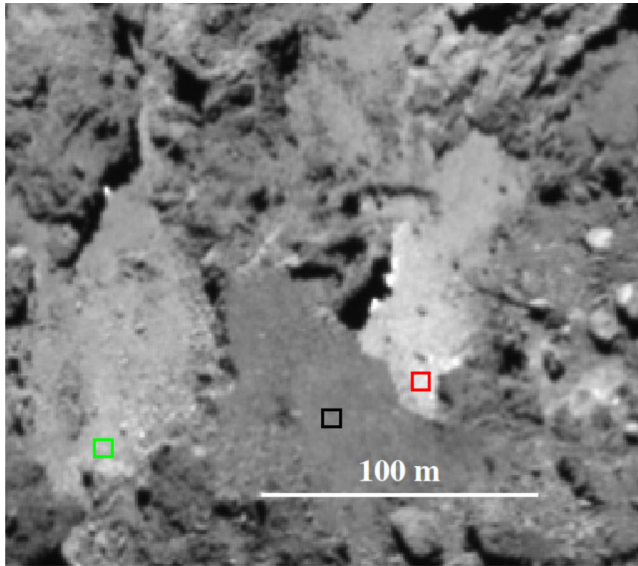
(a) Surface features selected from the Fig. 3d containing bluish material (red and green) and surrounding terrain (black). The marked boxes have the dimension of 7x7 pixels.
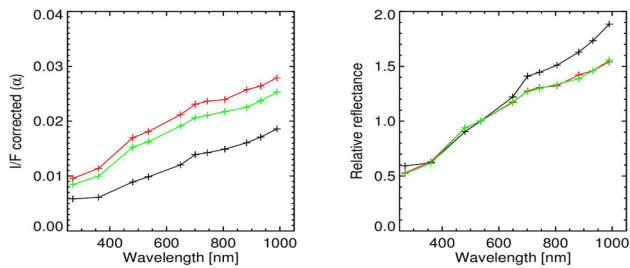
(b) Spectrophotometric plots for the selected features using an integration of 7x7 pixels as marked by the boxes in Fig. 4a

Figure 4. Spectrophotometric analysis of the bluish material seen in Fig. 3(d).

boulders inside the Khonsu region, we compared it to the power indices presented in Pajola et al. (2015). Their work offers three possible index ranges to explain the different boulder formation processes, i.e. a −5 to −6.5 power-law range, which can be attributed to collapses/pit formation and creation of depressions with subsequent escape of high-pressure volatiles and consequent high fracturing. A second power-law range, between −3.5 and −4.0, was suggested to be linked to gravitational events triggered by sublimation and/or thermal fracturing causing regressive erosion. A third power-law index range, between −1 and −2, was interpreted as the result of the evolution of the original material formed during both the collapsing or the gravitational event, not particularly renewed, or present in areas where continuous and high sublimation occurred or is still occurring (see fig. 8 of Pajola et al. 2016a). The geological analysis of this area (Lee et al., 2016) shows that different geological units are present here, such as talus deposits, fine material deposits, gravitational accumulation deposits as well as outcropping stratified terrains. Since the boulder analysis has been performed on the Khonsu physiographic region, we believe that the derived power-law index of −3.1 +0.2/−0.3 is indicative of all these different morphological units and the related formation processes, being slightly lower with respect to the −3.5 power-law index of
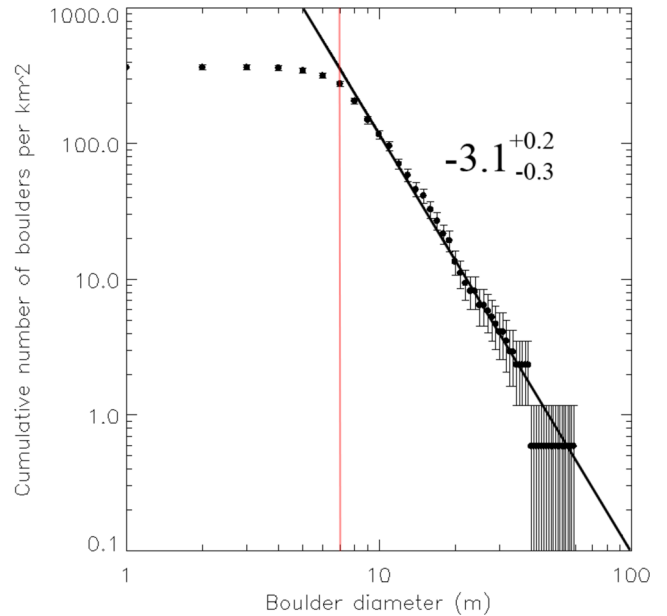

Figure 5. Cumulative SFD of boulders ≥7 m per km² over the Khonsu Region. Vertical error bars indicate the root of the cumulative number of counting boulders, divided by the area computed from the 3D shape model of the comet. The continuous line is a fitted regression line to the data, and the power-law index of the SFD is −3.1 +0.2/−0.3 computed in the range of 7–40 m. The bin size is 1 m and the red vertical line indicates the lower limit for the computation of the SFD power-law index.

purely gravitational deposits, but higher with respect to the −2.0 of collapsing events not particularly renewed by the retreating cliffs.

4 BRIGHT PATCHES IN KHONSU REGION

The detection of bright patches with high albedo characteristics on the comet 67P/C-G has triggered a growing discussion ever since Rosetta's arrival at the comet, when OSIRIS cameras started to observe them (Pommerol et al. 2015). They have been detected in different regions of the comet and we focus here on four bright patches that are evident in the OSIRIS images of the Khonsu region. Three of them fall into the category of isolated bright features that Pommerol et al. (2015) have introduced while one corresponds to a cluster of bright patches. Among these four, one patch observed from 2015 March to May has been associated within H_2O ice by Barucci et al. (2016) with complimentary infrared VIRTIS spectral data.

Fig. 6 shows the four bright patches in question and their observational conditions are given in Table 3. For each bright patch, the spectrophotometric plots make it clear that the absolute reflectance of the bright patch is considerably higher than that of the typical nucleus extracted from the neighbourhood of the bright patch. This implies a higher albedo for the considered feature and a compositional difference. All the four bright patches presented here seem to be tending towards a flat spectral behaviour, which is compatible with the characteristics of eight spots studied by Barucci et al. (2016), indicating the presence of H_2O ice. In this section, we treat each of the four bright patches individually by taking their temporal evolution of physical size and spectrophotometric properties into consideration, subject to the availability of data.
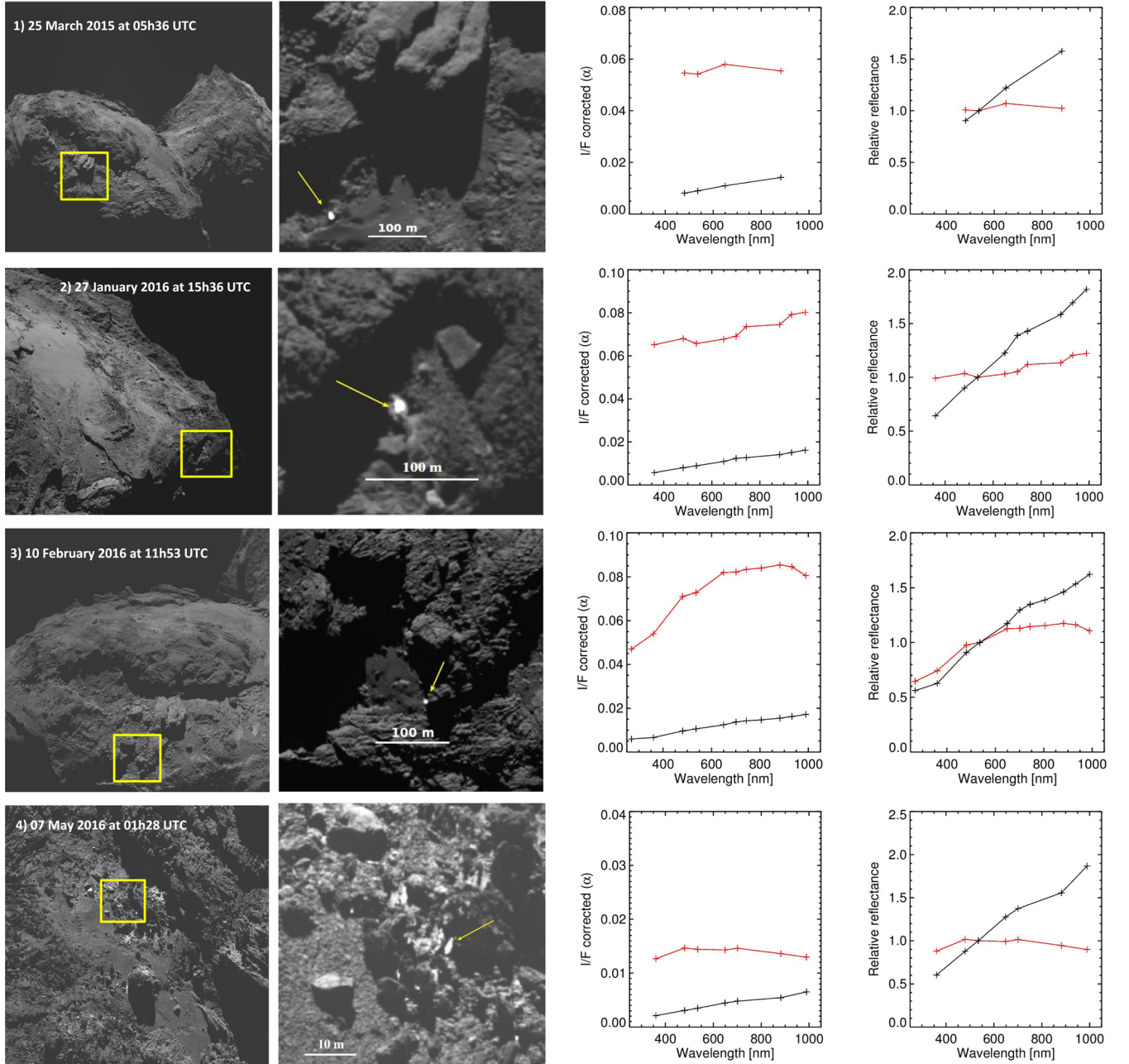
Figure 6. Four bright patches observed in Khonsu region and their spectrophotometric plots. For each bright patch, the leftmost panel shows the NAC reference image used for the analysis, along with a yellow square indicating the surface area used for a zoomed-in view as illustrated in the second panel from left. The third panel from the left shows the reflectance of the bright feature in red for the observed OSIRIS NAC filters, whereas the reflectance values of the typical nucleus extracted from the vicinity of the feature are indicated in black. The images used for this analysis are corrected for the illumination conditions using Lommel–Seeliger disc law. The rightmost panel presents the relative spectral behaviour with normalisation at the green filter centred at 535.7 nm. We remark that the absolute reflectances given in the plots for the bright patches 1, 2 and 4 are underestimated due to the saturation of few centre pixels resulting from high signal. After thorough scrutiny of individual pixels, the sampling for these three patches has been performed along their perimeters to avoid any contamination from saturated pixels. Therefore, the curves in question should be regarded as an indicative lower limit.

Table 3. Observational conditions for the four bright spots shown in Fig. 6. The column *S/R* refers to the spatial resolution and the southern latitudes are given with negative sign.

ID	Observation time	Altitude (km)	S/R (m pixel^{-1})	Approx. diameter (m)	Phase (°)	Lat (°)	Long (°)
1	2015-03-25_05h36	95.23	1.77	18.0	73.8	−23.80	198.30
2	2016-01-27_15h36	69.23	1.29	10.0	62.6	−13.32	196.47
3	2016-02-10_11h53	48.00	0.89	5.4	65.2	−18.73	196.48
4	2016-05-07_01h38	10.42	0.19	2.1	91.6	−24.23	200.42

Table 4. Temporal variation of the size of the bright patches 1 and 2 with their observational conditions. The column *S/R* refers to the spatial resolution.

| ID	Observation time	Approximate diameter (m)	*S/R* (m pixel^{-1})	Phase (°)	Filters	Filter wavelengths (nm)
1a	2015-03-10_18h40	8.5	1.56	53.8	3	[480.7,649.2,882.1]
1b	2015-03-25_05h36	18	1.77	73.8	4	[480.7,535.7,649.2,882.1]
1c	2015-04-12_21h42	8.0	2.75	80.5	11	[269.3,360.0,480.7,535.7,649.2,701.2,743.7,805.2,882.1,931.9,989.3]
1d	2015-05-02_13h42	7.0	2.29	60.6	11	[269.3,360.0,480.7,535.7,649.2,701.2,743.7,805.2,882.1,931.9,989.3]
1e	2015-05-07_17h43	5.2	2.62	61.4	4	[480.7,535.7,649.2,882.1]
1f	2015-05-22_21h04	0	2.33	60.0	11	[269.3,360.0,480.7,535.7,649.2,701.2,743.7,805.2,882.1,931.9,989.3]
2a	2016-01-23_23h45	8.0	1.34	61.2	3	[480.7,649.2,882.1]
2b	2016-01-28_02h49	10	1.29	62.6	9	[360.0,480.7,535.7,649.2,701.2,743.7,882.1,931.9,989.3]
2c	2016-03-02_06h35	9.8	2.46	92.0	1	WAC F18 [612.6]
2d	2016-05-03_01h00	5.8	1.72	90.8	1	WAC F21 [537.2]
2e	2016-06-24_20h28	3.8	1.92	87.1	1	WAC F12 [629.8]
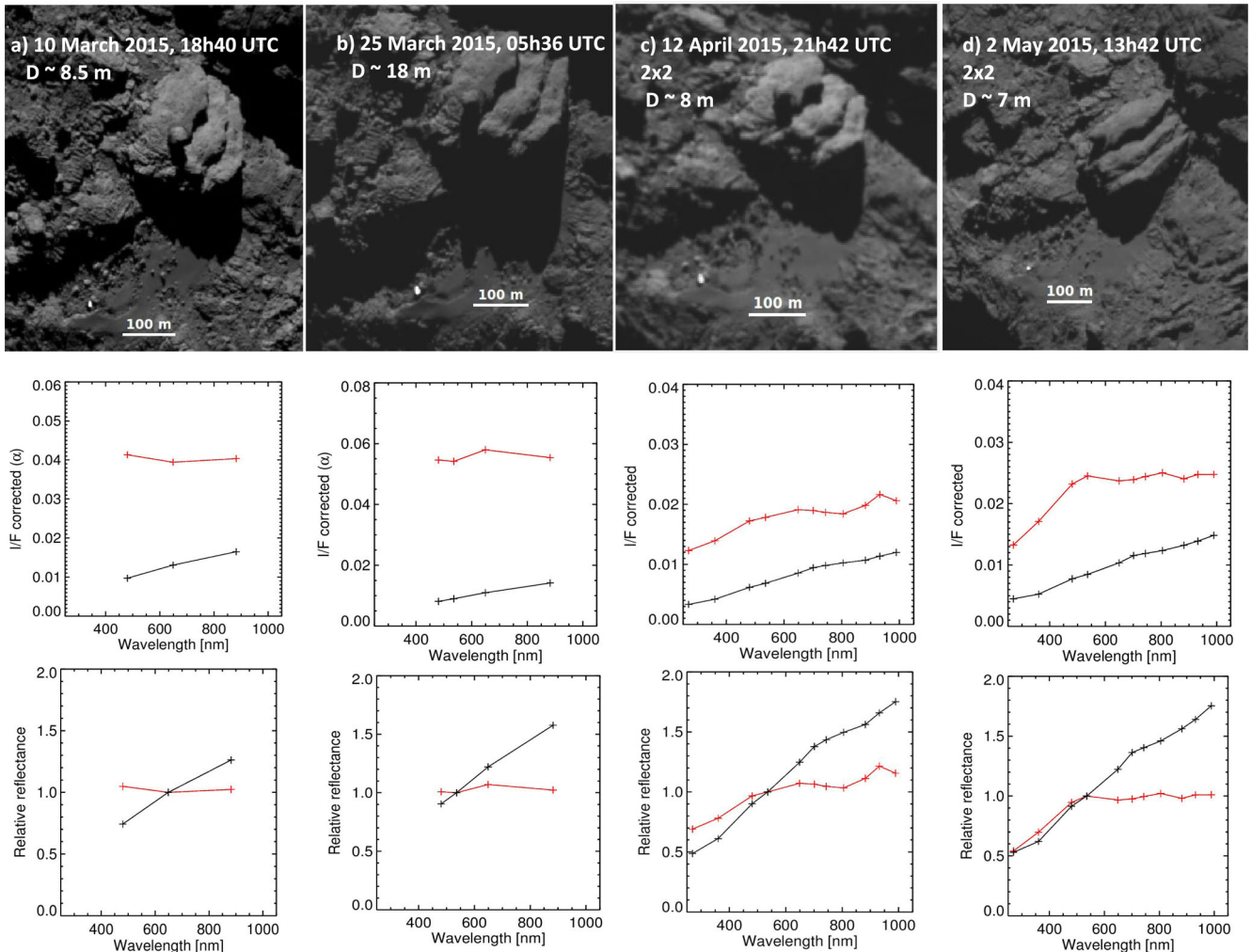
Figure 7. The top panel shows the temporal variation of the bright spot 1 during its observation and each of the temporal observation has its corresponding spectrophotometric plots below it. The observations are named according to the time they were made and corresponding dimensions of the bright patches are given as well as the pixel sampling criteria when available. The central and bottom panels give the spectrophotometric plots for the bright patch featured above them. The sequence 1c refers to the same observation of white spot ID 3 analysed and associated with H_2O ice by Barucci et al. (2016). As for the sub-figures a and b, we had to avoid the saturated centre pixels and hence sampling was done along the perimeter of the feature. Therefore, we remark that the absolute reflectances given in sub-figures a and b are underestimated and are to be considered as a lower limit.

Bright Patch 1.

First detected on 2015 March 10, this feature has been recorded multiple times in NAC, thus giving some insights about its temporal evolution in terms of size and spectrophotometric be-

haviour. It was under observation up to 2015 May 7 and seems to have disappeared by 2015 May 22. We list in Table 4 the temporal variation of the size of this bright patch with some other observational conditions and Fig. 7 shows cropped images
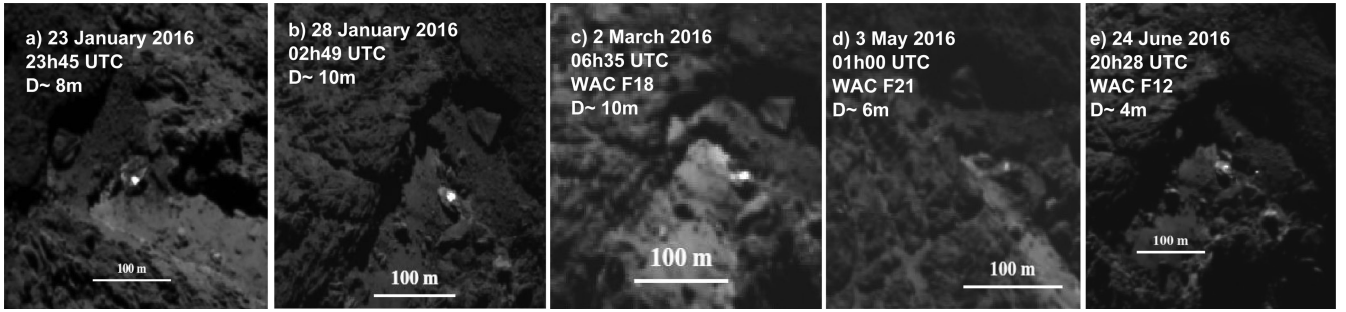
Figure 8. Temporal evolution of the bright patch 2 as seen from OSIRIS NAC and WAC images.

corresponding to some of the observations and spectrophotometric behaviour of the bright patch in comparison to that of the typical cometary nucleus.

From the obtained feature sizes during the observational span of about 2 months, it is clear that the feature had been undergoing a temporal evolution as explained by Barucci et al. (2016). One should also take into account the fact that the viewing geometry of each image is different and hence one must be cautious that the estimated dimension values might not correspond exactly to the real values of the feature at a given time and they should be considered as an approximative estimation. Given that this feature has a lifetime of about two months, we recall that Pommerol et al. (2015) have observed similar lifetimes for some of the bright patches they had catalogued. However, a direct comparison becomes tricky due to the different insolation conditions prevailed at corresponding heliocentric distances of the observations. We also highlight the spectrophotometric plots as given in Fig. 7 corresponding to the four selected sessions under observation. Their analysis is limited to the availability of filters for given circumstances, ranging from 3 to a favourable maximum of 11 filters depending on the session. The very high albedo (compared to the cometary nucleus) of the bright patch is emphasised in the two earlier observations (Figs 7a and 7b), while it seems to decrease towards the later (Figs 7c and 7d) observations. Barucci et al. (2016) have concluded that this bright patch contains H_2O ice using the infrared spectral data acquired from VIRTIS spectro-imager on-board Rosetta on 2015 March 25 and the high reflectance in our spectrophotometric plots is consistent with their interpretation of H_2O ice. The diminution of the reflectance can be explained as an aftermath of the sublimation of H_2O ice during constant solar insolation for over a month, leading the dirty ice (mixed with the nucleus material) to be more exposed. As seen in Fig. 7(d), this results in an important diminution of reflectance in ultraviolet wavelengths. The evolution of the physical dimensions of the bright patch contributes to the idea of sublimation of H_2O ice. As reported in Table 4, on 2015 May 7, we notice that this bright patch further continued to decay in its size and that it must probably have vanished completely between 2015 May 7 and May 22. We note that our analysis of the temporal evolution of this bright patch is consistent with that of Barucci et al. (2016) on the same spot (ID 3 among their eight white spots).

Bright Patch 2.

This bright patch can be seen sitting on a boulder or what appears to be a combination of a couple of boulders, resembling a boomerang. This configuration is often encountered at the surface of the nucleus, in various regions as shown, in particular, in

fig. 4 of Pommerol et al. (2015). This 'Boomerang' feature is located towards the very steep scarp that draws the border between Khonsu and Apis region. We see evidence that this bright patch has been stable for quite a long duration, far longer than the mean survival duration of most of the bright patches studied on the comet 67P/C-G. Its first detection dates to 2016 January 23 while its latest detection dates to 2016 June 24, which implies a lifetime of more than five months. Here, we used the OSIRIS WAC images to better constrain the lifetime of this bright patch and its temporal physical evolution can be seen in the Fig. 8, while its corresponding observational conditions are detailed in Table 4. As evident from the presented data, multispectral observations for this bright patch are only available at the early stages of detection. The three WAC observations we have only allow us to track the presence of the bright spot, but only limited information can be obtained due the lower spatial resolution of the WAC and the unavailability of multispectral data. Nonetheless, the multispectral observational sequence on 2016 January 27, as seen on Fig. 6, provided us with the spectrophotometric curves. In fact, the albedo of this bright patch was so high that most of its centre pixels were saturated. Consequently, we had to carefully sample the pixels, avoiding any saturated pixels for the spectrophotometric calculations. Therefore, we chose a 3×3 pixel box towards the perimeter of the patch where the signal was high but not saturated. From the absolute reflectance plot, it is clear that the signal of the bright patch is more than six times higher than that of the surrounding terrain. Interpreting the flat nature of the relative reflectance plot, we suggest that the source of this bright patch could plausibly be H_2O ice. The pixel saturation caused by the bright patch could be a clue to highlight the less contaminated nature of H_2O ice.

An interesting fact about this bright patch is that it could be related to a cometary outburst in the following way. The coordinates of this bright patch, 13°.32 of southern latitude and 196°.47 of longitude, thoroughly match those of the outburst identified by the ID 7 with $-12°$ of latitude and $196°$ of longitude by Vincent et al. (2016) in their catalogue of summer outbursts of 67P/C-G. This outburst dates to 2015 August 1 at 10h53 UTC and is likely to have triggered the appearance of the bright patch 2, after having altered the surface. In Fig. 9, we visualise the exact location with pre- and post-perihelion images in order to verify this idea. The figure clearly puts forward the idea that there has, in fact, been a considerable surface modification around the location identified by the coordinates. It is possible to discern few scattered boulders and outcroppings in the post-perihelion image. One can also notice that the terrace-like structure in the pre-perihelion image has vanished after the outburst event. Nevertheless, we note that this is only a correlation and the fact that we have not found any other mechanism
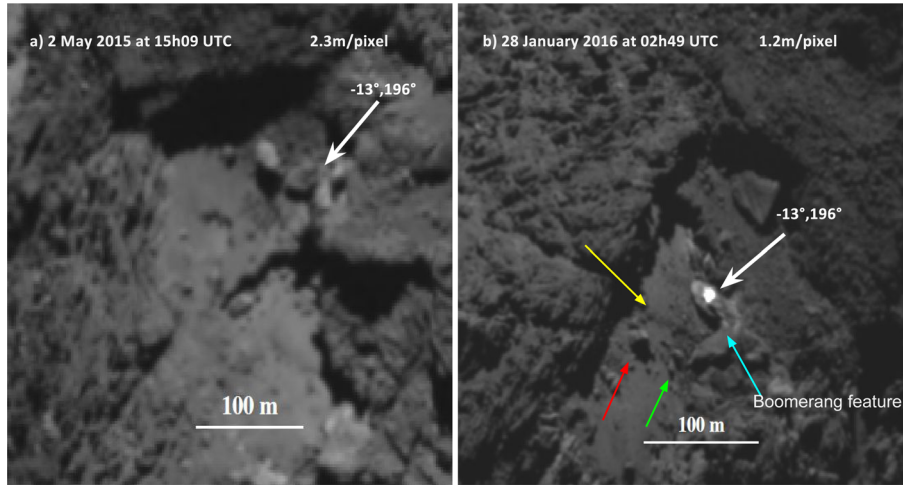
Figure 9. Left: the would-be location of the bright patch 2 before the perihelion passage. Right: location of the bright patch 2 on the 'Boomerang' feature after the perihelion passage. Few arrow identifiers are given where the red and green arrows point to some boulders, whereas the yellow arrow points to a terrace. The outburst that has potentially triggered the transition from a to b took place on the 2015 August 1, just about a fortnight before the perihelion passage at $-12°$, $196°$ coordinates.

to explain the surface modification does not rule out the possibility that this surface modification might have resulted from another mechanism.

Bright Patch 3.

This bright patch seems to be one of the short-lived bright patches as it has only been detected once. In fact, the follow-up observations did not show any more the existence of this bright patch. Given its smaller size, the preferable interpretation is that is has probably sublimated quickly. We remark that the spectrophotometric characteristics of this bright patch correspond to those of H_2O ice as shown by Barucci et al. (2016), as deduced from the flat nature of the corresponding curve in Fig. 6. It is noticeable also that the curve deviates from the flat behaviour towards ultraviolet wavelengths, following a pattern similar to the typical nucleus. This can be explained by considering the bright patch to be composed of H_2O ice and typical nucleus material. Since the size of the patch is quite small, there is probably the nucleus material dominating the signature of H_2O ice when co-registered and integrated.

Bright Patch 4.

Observed on 2016 May 7, this bright patch seems to be a part of a cluster of bright patches scattered near the 'pancake' feature in Khonsu region. Its individual size is smaller than the average isolated bright patches and is of the order of the scattered small bright patches observed elsewhere (Khepry, Imhotep regions) in the comet. The NAC images used for the spectrophotometry of this bright patch correspond to a spatial resolution of about 20 cm per pixel and hence offer the possibility to discern the bright patches quite well. An observation of the same area, after about 6 weeks, suggests that most of the small bright patches have already disappeared, for there seems to be only a single small bright patch of the original cluster that remains, with some bluish material lying alongside. Supported by the spectrophotometric plots of Fig. 6, we interpret this bright patch to contain H_2O ice. The high reflectance of this patch had, in fact, saturated the pixels in the centre, and we had to sample the pixels near its perimeter. From the location of this remaining bright patch, we could conclude that its existence has been favoured by the constant shadows. The existence of bright patches in a scattered form hints

that their origin might be different than that of the isolated bright patches.

5 DISCUSSION

Three of the studied bright patches on Khonsu are isolated, while one is a part of a cluster, although they might not share a common origin. As for the bright patch 2, we suggest that a cometary outburst had triggered it close to the perihelion passage, although it might have a different origin. This suggestion is supported by the fact that there has been a major surface modification after the outburst event. Furthermore, the bright patch 2 has been observed for a duration longer than five (Fig. 8) months. A bright patch with an area of about 80 m^2, maintaining its size for about a month and then getting halved at the end of the following two months, requires a mechanism to retain the bright patch without quick sublimation. This behaviour could be explained by the existence of sub-surface icy layers, which could compensate the H_2O ice being sublimated away. It is possible that the aforementioned outburst connected the plausibly underlying stratified ice layers in order for this process to work. We recall that a similar explanation was used by Barucci et al. (2016) to interpret the behaviour of their white spot 1. It is also noteworthy that the location of the bright patch 2 is often subject to shadows and hence the daily solar irradiation received at its location could be somewhat less than that for bright patch 1, whose location is not directly influenced by shadows as it is somewhat isolated on the smooth terrain on Khonsu. Therefore, we highlight that the location of the bright patch with regards to its neighbourhood is important to its survivability. The white spot 8 studied by Barucci et al. (2016) has been on the surface for more than four months and it was located between two boulders sitting next to each other, hence often casting shadows between themselves. In the case of bright patch 2 we present, it is next to the great scarp marking the Apis region, which results in constant shadows upon it.

Once again, we had to be cautious with the spectrophotometry of these bright patches, as often some of the centre pixels of the bright patches were saturated due to the high signal and we had to scrutinise the pixels before choosing them for the calculations. This implies an underestimation of the radiance factor of the

measurement and hence the plot should be considered only as an indicative lower limit. Even at saturation, the signal of bright patches was greater than that of the nucleus by a factor larger than 6. This means that the real factor would have been even larger. We recall that the normal albedo of 67P/C-G to be 6.8 per cent at 649 nm (Fornasier et al. 2015) and assuming a similar phase function between the dark terrain of the comet and the observed bright patches, we could estimate a normal albedo for the bright patches to be >40 per cent. Combining this estimation with the flat behaviour of the spectrophotometric curves, we could conclude that the source of these bright patches is plausibly freshly exposed H_2O ice.

6 CONCLUSIONS

We demonstrated that the composition of the Khonsu region is largely dominated by the desiccated refractory material with subtle spectrophotometric differences. The studied surface features, except the bright patches, show a red spectral behaviour, similar to what has been seen on the most of the other regions on the comet. General spectrophotometric characteristics of the Khonsu region relate to those of Anuket and Serqet regions, in comparison to the spectral slope work of Fornasier et al. (2015). We also note, in comparison with the work done by Fornasier et al. (2015) and Oklay et al. (2016), the presence of bluish material on Khonsu at different observation periods, relating to the spectrophotometric behaviour of Hapi region in the pre-perihelion period. Mainly dominated by H_2O ice, this bluish material has been observed more abundantly throughout the comet after the perihelion passage.

Our boulder analysis yields a power-law index of $-3.1 +0.2/-0.3$ that reflects a boulder formation shaped by varying geological processes for different morphological units. Present morphology of Khonsu region stands true to this by embodying a multitude of heterogeneous surface features. A higher resolution boulder identification analysis reaching minimum boulder dimensions close to 1–2 m is foreseen in the future, in order to extend this interpretation and to have wider statistics and focus on more localised areas inside this highly complex region of the comet.

We detected four bright patches associated with the presence of H_2O ice and two of them have shown long-term survivability, considering their location and size. We report that the larger bright patches under investigation have a life span of at least a couple of months, whereas the smaller ones last for a few weeks or fewer. We observe variations in the size of the two larger bright patches, with their sizes first increasing and then decreasing because of the diurnal and seasonal insolation conditions. The long-term survivability of the bright patches can be explained by the existing sub-surface ice layers, which could sustain them despite the ongoing sublimation. We also remark the estimation of >40 per cent of normal albedo for some bright patches, suggesting that they were composed of freshly exposed H_2O ice. The current spectrophotometric study of the bright patches and the terrain could be extended with the available observations and high-resolution images recorded during the later phases of the mission.

REFERENCES

Acton C. H., 1996, Planet. Space Sci., 44, 65
Barucci M. A., Dotto E., Levasseur-Regourd A. C., 2011, A&AR, 19, 48
Barucci M. A. et al., 2016, A&A, 595, A102
Bertin E., 2011, STIFF: Converting Scientic FITS Images to TIFF, Astrophysics Source Code Library, ascl:1110.006
Capaccioni F. et al., 2015, Science, 347, aaa0628
Ciarniello M. et al., 2015, A&A, 583, A31
El-Maarry M. R. et al., 2015, A&A, 583, A26
El-Maarry M. R. et al., 2016, A&A, 593, A110
Fairbairn M. B., 2005, J. R. Astron. Soc. Can., 99, 92
Fornasier S. et al., 2015 A&A, 583, 30
Fornasier S. et al., 2016, Science, 10.1126/science.aag2671
Jorda L., Spjuth S., Keller H. U., Lamy P., Llebaria A., 2010, in Computational Imaging VIII, p. 753311
Jorda L. et al., 2016, Icarus, 277, 257
Keller H. U. et al., 2007, Space Sci. Rev., 128, 26
Küppers M. et al., 2007, A&A, 462, 13
La Forgia F. et al., 2015, A&A, 583, 41
Lee J.-C. et al., 2016, MNRAS, in press
Lucchetti A. et al., 2016, A&A, 585, 1
Massironi M. et al., 2015, Nature, 526, 402
Nyquist H., 1928, Trans. Am. Inst. Electron. Eng., 47, 617
Oklay N. et al., 2016, A&A, 586, 80
Pajola M. et al., 2015, A&A, 583, A37
Pajola M. et al., 2016a, A&A, 592, A69
Pajola M. et al., 2016b, A&A, 592, L2
Pommerol A. et al., 2015, A&A, 583, 25
Sierks H. et al., 2015, Science, 347, aaa1044
Thomas N. et al., 2015, Science, 347, aaa0440
Tubiana C. et al., 2015, A&A, 583, 46
van der Walt S. et al., 2014, PeerJ 2:e453
Vincent J.-B. et al., 2016, MNRAS, in press

[1]*LESIA, Observatoire de Paris, CNRS, UPMC Univ. Paris 06, Univ. Paris-Diderot, 5 Place J. Janssen, F-92195 Meudon Principal Cedex, France*
[2]*Max-Planck-Institut für Sonnensystemforschung, Justus-von-Liebig-Weg, 3, D-37077 Göttingen, Germany*
[3]*Physikalisches Institut, Sidlerstrasse 5, University of Bern, CH-3012 Bern, Switzerland*
[4]*NASA Ames Research Center, CA 94035, USA*
[5]*Department of Physics and Astronomy 'G. Galilei', University of Padova, Vic. Osservatorio 3, I-35122 Padova, Italy*
[6]*Laboratoire d'Astrophysique de Marseille UMR 7326, CNRS and Aix Marseille Université, F-13388 Marseille Cedex 13, France*
[7]*Centro de Astrobiología, CSIC-INTA, E-28850 Torrejón de Ardoz, Madrid, Spain*
[8]*International Space Science Institute, Hallerstrasse 6, CH-3012 Bern, Switzerland*
[9]*Research and Scientific Support Department, European Space Agency, NL-2201 Noordwijk, the Netherlands*
[10]*Department of Physics and Astronomy, Uppsala University, SE-75120 Uppsala, Sweden*
[11]*PAS Space Reserch Center, Bartycka 18A, PL-00716 Warszawa, Poland*

[12]*Department for Astronomy, University of Maryland, College Park, MD 20742-2421, USA*

[13]*LATMOS, CNRS/UVSQ/IPSL, 11 Boulevard d'Alembert, F-78280 Guyancourt, France*

[14]*INAF–Osservatorio Astronomico di Padova, Vicolo dell'Osservatorio 5, I-35122 Padova, Italy*

[15]*CNR-IFN UOS Padova LUXOR, Via Trasea 7, I-35131 Padova, Italy*

[16]*JPL, 4800 Oak Grove Drive,Pasadena,CA 91109, USA*

[17]*Department of Mechanical Engineering – University of Padova, Via Venezia 1, I-35131 Padova, Italy*

[18]*UNITN, Universitá di Trento, Via Mesiano, 77, I-38100 Trento, Italy*

[19]*INAF – Osservatorio Astronomico di Trieste, via Tiepolo 11, I-34143 Trieste, Italy*

[20]*Instituto de Astrofísica de Andalucía – CSIC, E-18080 Granada, Spain*

[21]*Institute of Planetary Research, DLR, Rutherfordstrasse 2, D-12489 Berlin, Germany*

[22]*Institute for Space Science, National Central University, 32054 Chung-Li, Taiwan*

[23]*Institute for Geophysics and Extraterrestrial Physics, TU Braunschweig, D-38106 Braunschweig, Germany*

[24]*ESA/ESAC, PO Box 78, E-28691 Villanueva de la Cañada, Spain*

[25]*Department of Information Engineering – University of Padova, Via Gradenigo 6, I-35131 Padova, Italy*

[26]*Center of Studies and Activities for Space (CISAS) 'G. Colombo', University of Padova, Via Venezia 15, I-35131 Padova, Italy*

This paper has been typeset from a TEX/LATEX file prepared by the author.